



CHALMERS
UNIVERSITY OF TECHNOLOGY

Three-dimensional reconstruction and computational analysis of a structural battery composite electrolyte







Downloaded from: <https://research.chalmers.se>, 2026-04-04 01:15 UTC

Citation for the original published paper (version of record):

Duan, S., Cattaruzza, M., Tu, V. et al (2023). Three-dimensional reconstruction and computational analysis of a structural battery composite electrolyte. *Communications Materials*, 4(1). <http://dx.doi.org/10.1038/s43246-023-00377-0>

N.B. When citing this work, cite the original published paper.

Three-dimensional reconstruction and computational analysis of a structural battery composite electrolyte

Shanghong Duan¹, Martina Cattaruzza ², Vinh Tu ¹, Robert M. Auenhammer¹, Ralf Jänicke ³, Mats K. G. Johansson ², Fang Liu ¹ & Leif E. Asp ¹✉

Structural batteries are multifunctional composite materials that can carry mechanical load and store electrical energy. Their multifunctionality requires an ionically conductive and stiff electrolyte matrix material. For this purpose, a bi-continuous polymer electrolyte is used where a porous solid phase holds the structural integrity of the system, and a liquid phase, which occupies the pores, conducts lithium ions. To assess the porous structure, three-dimensional topology information is needed. Here we study the three-dimensional structure of the porous battery electrolyte material using combined focused ion beam and scanning electron microscopy and transfer into finite element models. Numerical analyses provide predictions of elastic modulus and ionic conductivity of the bi-continuous electrolyte material. Characterization of the three-dimensional structure also provides information on the diameter and volume distributions of the polymer and pores, as well as geodesic tortuosity.

¹Chalmers University of Technology, Department of Industrial and Materials Science, SE-412 96 Gothenburg, Sweden. ²KTH Royal Institute of Technology, Department of Fibre and Polymer Technology, KTH Royal Institute of Technology, SE-100 44 Stockholm, Sweden. ³Technische Universität Braunschweig, Institute of Applied Mechanics, Pockelsstraße 3, 38106 Braunschweig, Germany. ✉email: leif.asp@chalmers.se

Energy storage materials have gained wider attention in the past few years. Among them, the lithium-ion battery has rapidly developed into an important component of electric vehicles¹. Structural battery composites are one type of lithium-ion batteries that employs carbon fiber as the negative electrode². Since carbon fiber is an excellent lightweight structural reinforcement material the structural battery composite inherits high mechanical properties³. A successful example is a recently reported structural battery by Asp et al.⁴ and its integration in a multi-cell composite laminate⁵. The structural battery possesses an elastic modulus of 25 GPa and strength of 300 MPa and holds an energy density of 24 Wh kg⁻¹. With its combined energy storage and structural functions, the structural battery provides massless energy storage. Replacing parts of the structural components in various applications, such as electric vehicles, the weight of the whole system is reduced^{6,7}.

In order to carry mechanical loads, the structural batteries must be of high stiffness. Structural electrodes are generally utilizing carbon fibers^{2,8}. In the negative electrode, carbon fibers are used as active material, i.e., host of lithium, current collector, and reinforcement^{6,9}. In the positive electrode, active material, e.g., lithium iron phosphate is coated on the carbon fiber that acts as a current collector and reinforcement^{10,11}. For the same reason, the liquid electrolyte in conventional lithium-ion batteries cannot be used and must be replaced by a mechanically robust, at least partly solid, electrolyte system. Solid inorganic electrolytes have high ionic conductivity ($>10^{-4}$ S cm⁻¹) and high elastic modulus (>1 GPa)¹². However, their poor interfacial properties and fragility cause difficulties in practical use. Solid polymer electrolytes and gel electrolytes are not well fit in structural battery either, since their mechanical and electrochemical properties are highly antagonistic¹³. In the recent structural battery, a bi-continuous polymer structural battery electrolyte (SBE) is used⁴. Its porous structure is formed by polymerization-induced phase separation (PIPS) reaction¹⁴. The solid polymer backbone ensures the integrity of the entire structure, whereas the liquid electrolyte, which occupies the porous network structure, allows the transport of lithium ions. This SBE structure offers a good compromise between ionic conductivity ($\sim 2 \times 10^{-4}$ S cm⁻¹) and mechanical properties (elastic modulus of 540 MPa).

Further development of the SBE requires a deep understanding of its structure and an accompanying structure-property relationship analysis. For a porous structure, traditional two-dimensional (2D) images from scanning electron microscopy (SEM) are not sufficient. Instead, a three-dimensional (3D) model is required to analyze the mechanical properties and ionic conductivity of the porous network via numerical simulations. X-ray computed tomography is a popular non-destructive method to obtain 3D structure information. Its spatial resolution can be down to 50 nm, which is not sufficient to accurately capture the nano-scale pores in the SBE¹⁵. Instead, combined focused ion beam and scanning electron microscopy (FIB-SEM) is utilized. FIB-SEM is nowadays a well-established technique to obtain high-resolution 3D data. Serial milling using FIB can be performed at the nanometer scale to expose the underlying micro-structure. High-resolution 2D images are then taken by SEM. The obtained 2D image sequences are stacked in 3D space. Different phases are separated, and 3D voxel models are generated for the different phases. This technique has been successfully used in studies of different porous structures^{16–20}. However, FIB-SEM has not yet been applied to the SBE, which is more challenging since the SBE is a soft and non-conductive material. These features cause issues such as curtaining, charging, and low contrast of images^{19–23}. In general, artifacts induced by FIB milling on such specimens are more conspicuous and can be compensated for in the analysis. Furthermore, the pores in the SBE are very

small, ranging from a few to hundreds of nanometers. Most previous studies investigated micro-scale pore structures. However, Neusser et al. performed FIB-SEM on soft polymer MIP at the nano-scale²³. To enhance contrast, the polymer structure was stained with osmium tetroxide and then filled with epoxy. In the current study, we take high-resolution SEM images using the so-called electron immersion mode where electrons are caged in the imaging region. The pixel size in the SEM image can be as low as 5 nm, which determines the achievable resolution in the image, whereas the resolution through the thickness is determined by the FIB-milling depth. Pores smaller than achievable resolution cannot be captured by the proposed FIB-SEM technique.

In the present work, we aim to develop a general workflow to reconstruct a porous glassy polymer and analyze its structure and effective properties, namely ionic conductivity and elastic stiffness. High-resolution images are taken using FIB-SEM to generate 3D models of the polymer and pore phases of the SBE. With these models, the pore size distribution and tortuosity are analyzed. Also, the geodesic distance is measured and related to the Euclidean length. Furthermore, the reconstructed 3D models are used to generate finite element models of the two phases. The elastic modulus and ionic conductivity are experimentally measured and numerically simulated, and the results are compared and discussed. The developed method can be used to analyze porous polymers, e.g., SBE with different compositions and interfaces.

Results and discussions

Three-dimensional reconstructions. 3D models of the SBE are reconstructed as illustrated in Fig. 1a. High-resolution micrographs of the SBE were first obtained from FIB-SEM as illustrated in Fig. 1b. Reconstruction of the SEM images was achieved using the Dragonfly 2020.2 software. Filtering processes were conducted to reduce a strong curtaining effect and noise in the SEM images. The curtaining effect is a common artifact induced by FIB milling^{24–27} and appears as vertical stripes on the cutting surface, as shown in Fig. 1c. The stripe pattern is caused by different milling rates at different positions, i.e., in the polymer and the pore phases of the porous structure. The curtaining artifact causes erroneous image segmentation and must therefore be removed. As shown in Fig. 1c, the curtaining effect is effectively removed through a dstripie filter. Gaussian smoothing filter is then applied in 3D space to reduce the noise pixels.

Even though the SEM images are automatically aligned according to a reference pattern during FIB-SEM sectioning, alignment error can still be observed as shown in Fig. 1d. Therefore, a box region of the image stack is used to perform additional alignment. The additional image alignment is performed to correct the distorted pore shapes in a registration step (Fig. 1d) as described in the Method section. The edge of the SBE sample is a tilting line due to the sample placement angle. Thereafter, the pore and polymer pixels are separated by threshold segmentation. The transition regions between polymer and pore phases are a few pixels due to the low contrast, different depths of the pores, and charging at the pore edges. The best option is to use the true porosity instead of an arbitrary threshold. However, experimental measurements of the porosity of a porous polymer system in the meso-range are difficult. For example, Brunauer–Emmet–Teller (BET) theory relies on the Langmuir assumption that gas molecules form monolayer adsorption, which is an ideal situation²⁸. Furthermore, the assessment of meso-porosity relies on the assumption that the pores are filled with the adsorbate in the bulk liquid state, i.e., by applying the Gurvich rule, only if the mesoporous adsorbent contains no macropores²⁹. Clearly, these assumptions do not apply to the studied SBE system. Therefore, the porosity of the SBE is calculated from the volume ratio of liquid electrolyte and monomer in the SBE mixture

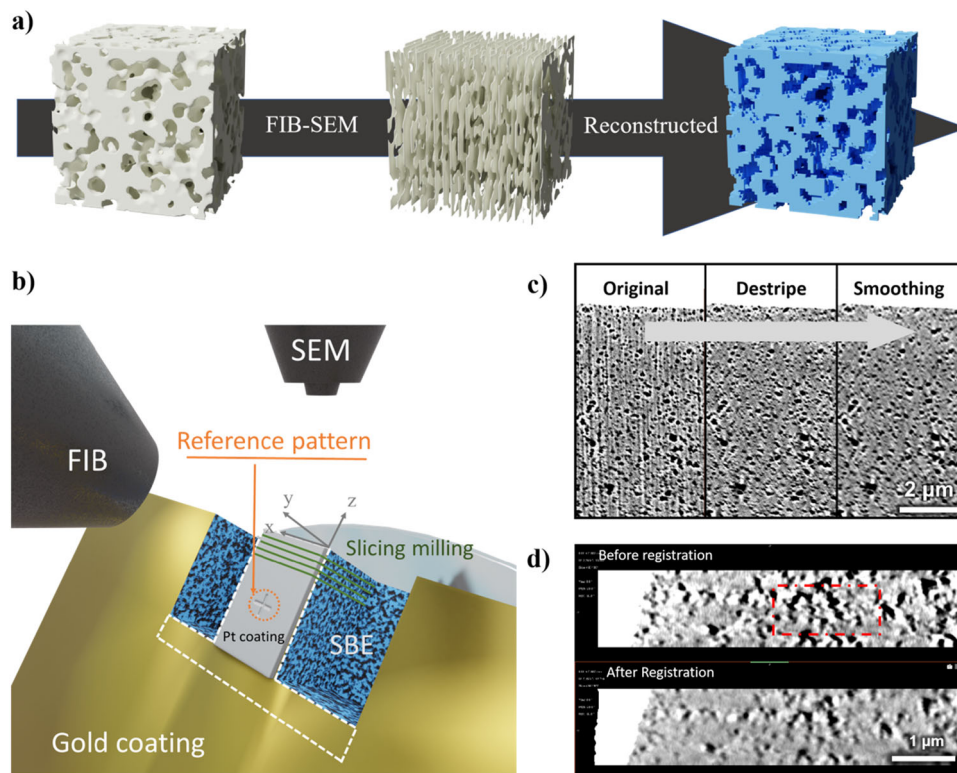


Fig. 1 Three-dimensional reconstruction of the SBE. **a** Illustration of 3D reconstruction of the SBE model. **b** Illustration of the FIB-SEM set-up. **c** Effects of destriping and Gaussian smoothing on image quality. **d** The y-view of a cross-section of the image stack. The pore shapes are distorted in the same way in the red box. The registration step realigns the image positions as the left edge is no longer straight.

before curing. The liquid content in the mixture was 45 wt%, which corresponds to a volume fraction of 41%. A recent study on the bulk polymer of the SBE, using the nuclear magnetic resonance (NMR) technique, shows between 8 to 10 % of the liquid electrolyte to be absorbed in the bulk polymer³⁰. The porosity in the SBE is therefore in the range of 37–38%. Here, a threshold value for segmentation is set to match a porosity of 37%. To obtain the polymer 3D model, the pore pixels are removed, and the polymer pixels are then transformed into voxels with a thickness of 20 nm. In the final step, the obtained 3D models are stretched by 22% in the y-direction to compensate for the view angle of 55° between the FIB milled cross-section and the SEM (Fig. 1b).

The 3D models generated from the SEM image stack, representing the polymer phase, and the pore phase, and both phases are shown in Fig. 2a–d. The pixel size in the micrographs is $10 \times 10 \text{ nm}^2$. Each pixel is converted into a voxel volume of $10 \times 12.2 \times 20 \text{ nm}^3$. The volume is not square in the x-y plane due to the view angle of the milled surface in the SEM. The polymer phase is marked in blue and the pore phase in orange. In total, the studied volume is approximately $5.43 \times 6.31 \times 1.20 \mu\text{m}^3$. The pores with a size smaller than 20 nm will unfortunately not be identified. However, the impact of such small pores on the elastic properties can be neglected. In contrast, the effect of neglecting small pores on ionic conductivity predictions is more ambiguous. On the one hand, ionic conductivity is expected to be controlled by the connected network of large pores. Also, the undetected small pores are likely to be isolated from the connected network. Cattaruzza et al. explored SBE with different porosity and found the interactions between the electrolyte species and the polymer matrix hinder the molecule and ions transport³⁰. On the other hand, if the amount of non-identified small pores is large enough, the volume of the network of connected large pores, and hence the ionic conductivity, will be overestimated.

Although some pores appear isolated on the surface of the 3D model (Fig. 2d), 99.3% of the pores are connected in space. The isolated pores are determined by a 6-connected analysis. Thus, if any of the six faces of a voxel is shared with another voxel, the two voxels are identified as being connected. The isolated pores are marked by light blue in Fig. 2e. However, it is worth to note that the isolated pores on the surface are probably connected to other pores outside the reconstructed volume. To study the distribution of polymer and pore size, connected voxels are separated into individual elements. This is done by creating a multi-ROI (region of interest) using the OpenPNM plugin³¹.

As shown in Fig. 3a, b, individual polymer segments and pores, respectively, are marked with a different color from its neighbors. The distributions of equivalent diameter and volume of polymer segments and pores are plotted in Fig. 3d, e. The mean equivalent diameter is found to be 180 nm for the polymer segments and 160 nm for the pores, respectively.

Geodesic tortuosity. When lithium ions move through the porous SBE a straight and direct path is not available. To evaluate the path distances traveled by the ions in the SBE structure, sparse and dense graphs are generated from the pore model (Fig. 4a, b). Sparse and dense graphs are connected models using spheres representing pore areas and lines for paths between pore volumes. The zoom-in views of a small region show that the dense graph gives detailed information on the distorted paths, whereas the sparse graph, a lower resolution version, simply connects pore nodes with linear paths. From the dense graph, an average segment tortuosity of 1.3 is computed. The segment tortuosity is defined as the ratio of the tortuous path distance to the Euclidean distance of one segment. Since different segments are not aligned, segment tortuosity does not provide enough information to assess ion transport. Hence, ion transport through multi-segments needs to be further evaluated.

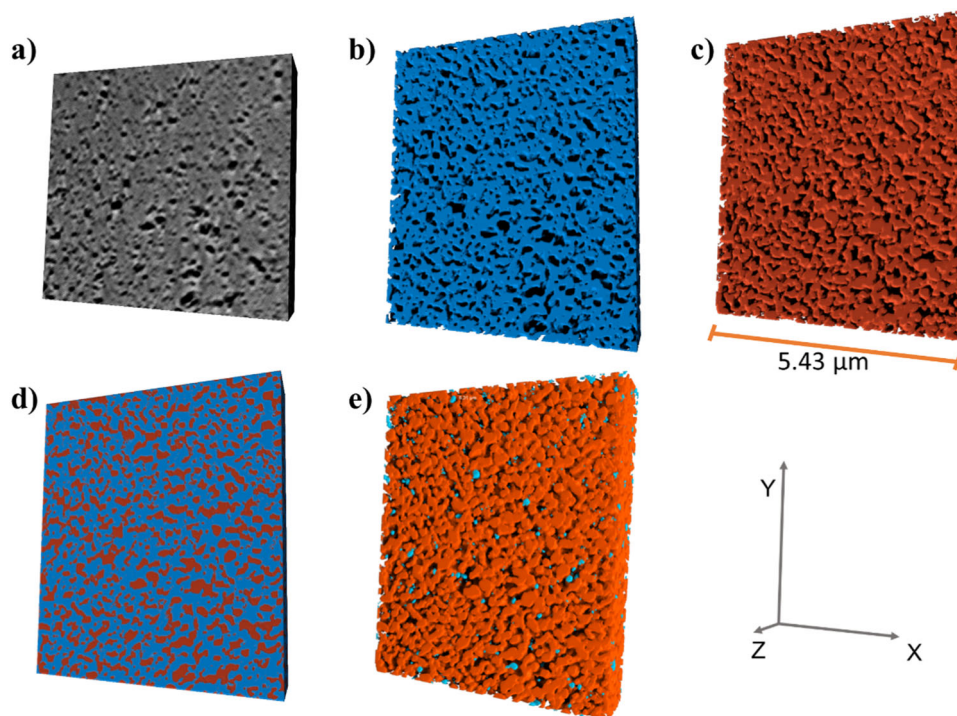


Fig. 2 Reconstructed material models. 3D visualizations of **a** the unstretched SEM image stack. The final stretched models for **b** the polymer phase, **c** the pore phase, **d** both polymer and pore phases, and **e** isolated (light blue) and connected (orange) pore regions.

Geodesic tortuosity is the ratio of the shortest path to the Euclidean distance between two vertices. To compute the shortest paths, cuboid lattices are defined in the sparse and dense graphs, respectively. Two different vertices are selected at the two ends of lattices as inlet and outlet. The shortest paths are computed between the inlet and the outlet vertices and marked in yellow in Fig. 4d. The geodesic tortuosity is studied using both the dense graph and the sparse graph (Table 1). The dense graph gives a longer shortest distance compared to the sparse graph. Obviously, the higher resolution of the dense graph gives a more accurate result compared to the sparse graph. In the y-direction, the average geodesic tortuosity measured in the dense graph is 1.81. This means that the lithium ions need to travel a 1.81 times longer distance in the SBE than the Euclidean distance. When the shortest path between two vertices is computed from the dense graph, with its highly tortuous segments, a 30% longer distance results compared to if it is computed from the linear segments in the sparse graph. This is schematically illustrated in Fig. 4c. From a statistical point of view, the ratio between the red and orange path lengths in Fig. 4c should be equal to the average segment tortuosity given a sufficient number of segments are included. Therefore, the geodesic tortuosity from the sparse graph is computed by multiplying the shortest distance by the segment tortuosity of 1.3. The geodesic tortuosity from the sparse graph is slightly higher than that from the dense graph because more available path choices exist in the dense graph. However, the computational cost of the dense graph is approximately 30 times higher than that of the sparse graph. Therefore, it is an efficient method to use the sparse graph to analyze the geodesic tortuosity. A slightly lower tortuosity is measured in the z-direction. This is likely caused by the lower voxel resolution of the 3D model in the z-direction, where highly tortuous paths are lost. The geodesic tortuosity is similar in all three directions, which confirms the isotropy of the SBE. An average geodesic tortuosity of 1.8 is measured, based on measurements on six, five, and eight paths in x-, y-, and z- directions, respectively.

Multifunctional properties of the SBE. We exploit the obtained topology data to numerically compute both, elastic modulus, and ionic conductivity, and compare the simulation results with experimental results. The results are reported in Table 2. Dynamic mechanical analysis (DMA) and electrochemical impedance spectroscopy (EIS) were performed to measure the storage modulus and the ionic conductivity, respectively. The experimental results are plotted in Fig. 5a, b. The measured elastic modulus of the bulk polymer is 2167 MPa and the ionic conductivity of the liquid electrolyte is 4.35 mS m^{-1} . These measured properties are used as input properties for the finite element method (FEM) analyses based on linear elasticity and linear Fickian diffusion³². In addition, a Poisson's ratio of 0.33 is imposed for the polymer phase. In the FEM analyses it is assumed that the elastic modulus relies only on the polymer and that ionic conductivity is solely attributed to the liquid phase. In total, 20 unique cubical statistical volume elements (SVEs), with a volume of approximately $1.2 \mu\text{m}^3$, were extracted from the reconstructed 3D model and analyzed (Fig. 5c). One example SVE of each phase (solid and liquid) is shown in Fig. 5d, e. The simulation results presented in Table 2 are ensemble averages from the simulation results of all 20 SVEs.

The average effective elastic modulus of the SBE from numerical simulations is 738 MPa. The predicted modulus is slightly higher than the measured modulus of 611 MPa. This discrepancy can be explained by the usage of Dirichlet boundary conditions during virtual material testing in the FEM simulations. Dirichlet boundary conditions are known to slightly overestimate the elastic modulus. Nevertheless, the simulation and experimental results agree well for elastic modulus. In contrast, for the ionic conductivity, the FEM simulation overestimates the performance of the SBE. There are a few reasons for this. Firstly, the resolution in the extracted image data is in the range of 10 to 20 nm. Consequently, any pores smaller than 10 nm are not identified and therefore not introduced in the 3D model. Therefore, the numerical models likely consider too coarse pore structures for the given porosity, leading to overestimated ionic conductivity. Secondly, it should be noted that the

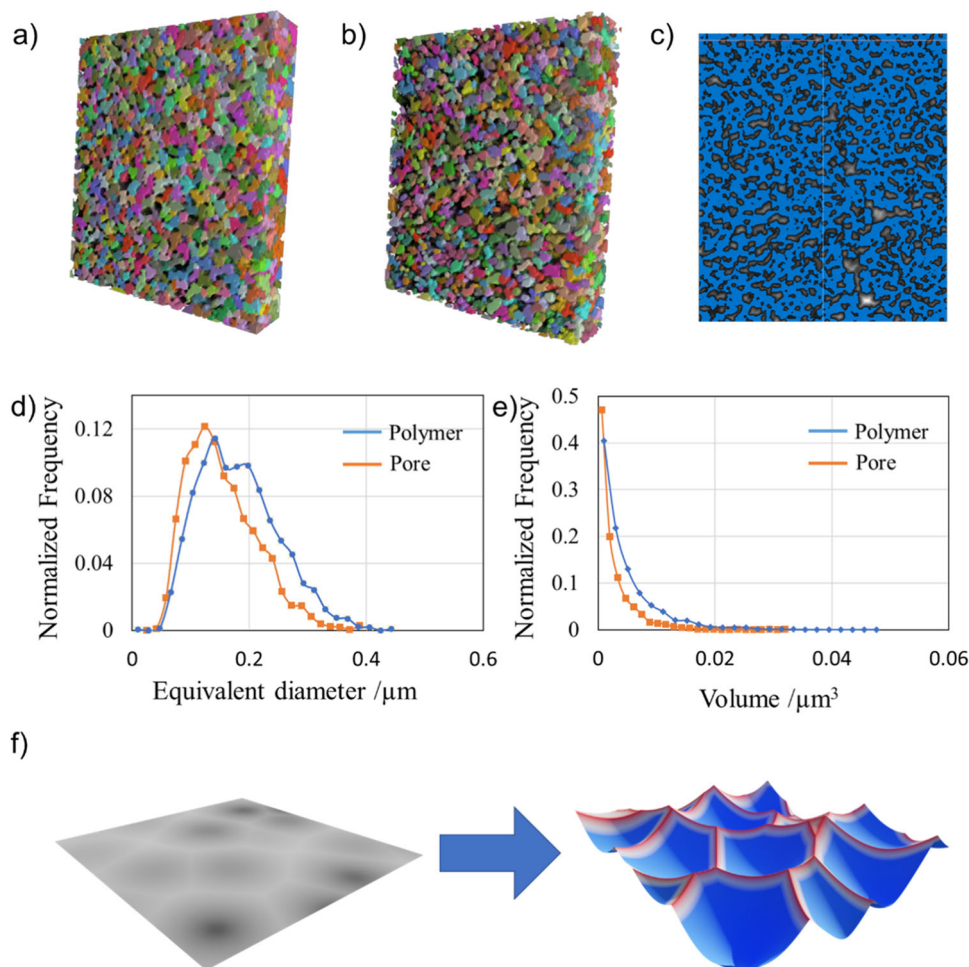


Fig. 3 Pore structure of the SBE. **a** Segmented polymer model. **b** Segmented pore model. **c** Distance map of the pores (grayscale) in the polymer model (blue). **d** The distributions of equivalent diameter, and **e** volume of the polymers and pores. **f** In the watershed algorithm, the brightness of a grayscale image is treated as height information. The grayscale image is transferred to a 3D terrain, where the red lines are ridges, and the blue regions are catchment basins.

FIB/SEM reconstructed model is from a dry specimen, whereas the measured performance is for a specimen in its wet state. In the wet state, the polymer is expected to absorb some of the liquid electrolytes and operate in a swollen state. A swollen polymer backbone results in lower porosity, lower liquid content, and some narrow path channels may even be closed. All these features can contribute to a reduced ionic conductivity of the wet SBE. On the other hand, the current FEM model only considers Fickian diffusion. Other possible phenomena like convection and the interaction between ions are not included. An issue with the FEM simulations is that the SVEs have slightly varying volume fractions depending on where they are sampled from on the specimen. This volume fraction variation can reach up to a 10 % difference between the SVE outliers. However, these fluctuating effects are averaged out as the FEM simulations are repeated for twenty different SVEs. This shows the importance of using sufficiently large SVEs. A clear opposing relationship between elastic modulus and ionic conductivity to the ratio of the solid to liquid phases is found, as shown in Fig. 5f, g.

Conclusion

Here, we characterize the geometry of a porous structural battery electrolyte (SBE) in three dimensions and predict its multi-functional properties, i.e., elastic modulus and lithium-ion

conductivity. Sequential FIB-SEM milling is used to obtain a stack of high-resolution images for the porous electrolyte matrix. An efficient image processing routine is reported. The pore and polymer phases are segmented, and 3D reconstructed. The individual pores/polymer diameter and volume distributions are analyzed, and the average diameter of the pores and the polymer backbone is found to be 160 to 180 nm, respectively. To assess the lithium-ion conductivity of the SBE structure, geodesic tortuosity is computed by the shortest path and found to be isotropic. The average geodesic tortuosity indicates that the lithium ions need to travel 1.8 times longer distances in the porous SBE compared to the spatial Euclidean distance. In addition, the 3D model is used to generate finite element models to compute the elastic modulus and ionic conductivity of the SBE. The predicted elastic modulus agrees well with the measured storage modulus of the SBE. In contrast, the computational model overestimates lithium-ion conductivity. This can be due to the limitation posed by the use of a dry specimen in the current FIB-SEM experimental set-up and to the limiting resolution of the extracted image data. Further work is needed to allow for the characterization of the wet SBE. Nevertheless, the presented experimental and computational procedure can be applied for the study of arbitrary compositions of SBE and provides a foundation for future study of SBE and structural electrode interface regions.

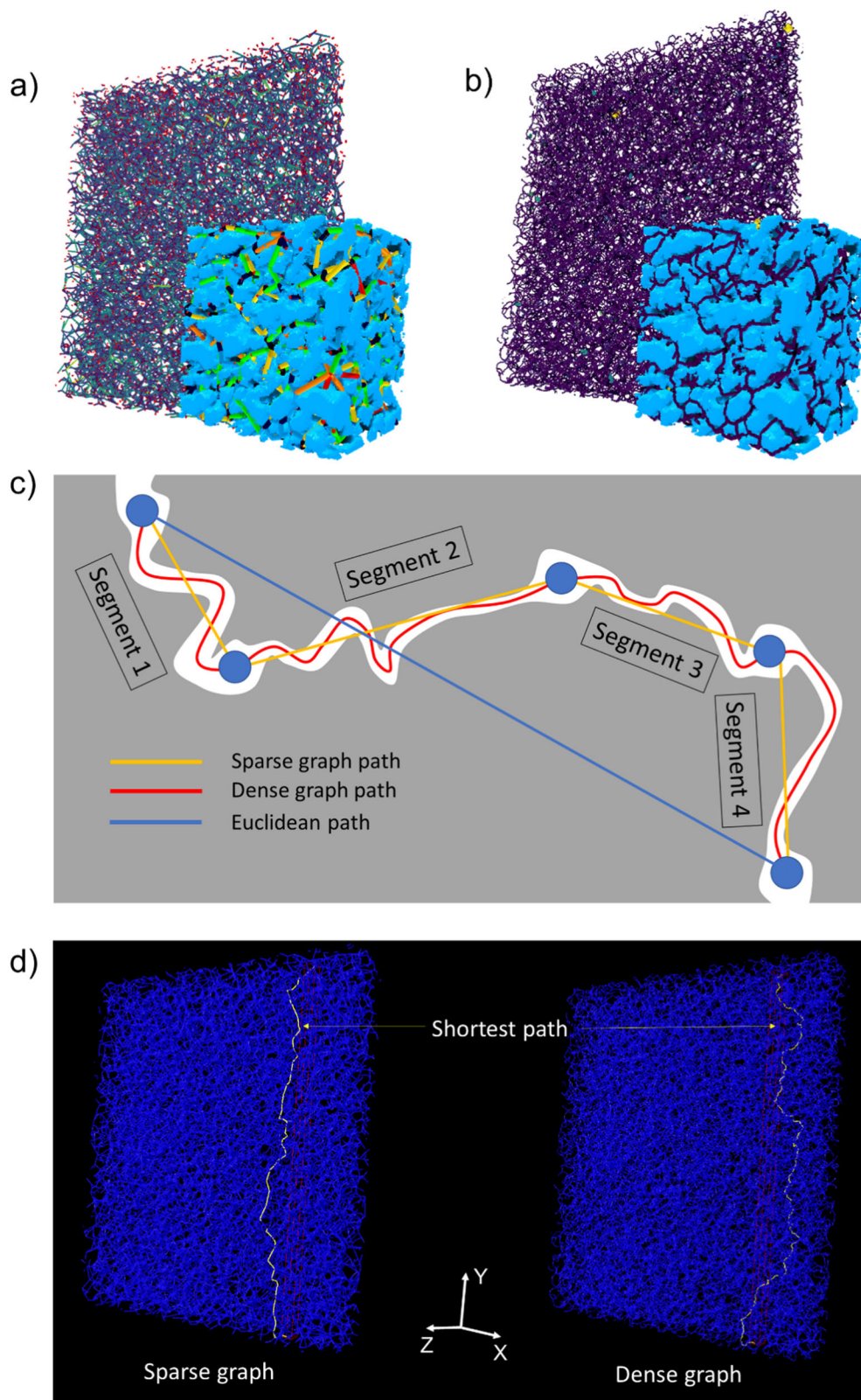


Fig. 4 Geodesic tortuosity. The **a** sparse and **b** dense graph pore models combined with a zoom-in view with the polymer model. **c** Illustration of the sparse and dense graph paths. **d** The shortest paths computed from the sparse and dense graphs.

Methods

Sample preparation. The SBE was cured from a solution mixture of self-made liquid electrolyte (45 wt%) and monomer Bisphenol A ethoxylate dimethacrylate (M_n : 540 g mol^{-1}) from Sartomer Europe. The liquid electrolyte solvent is a 1:1 weight ratio mixture of propylene carbonate (PC $\geq 99\%$, acid < 10 ppm, H_2O < 10 ppm)

(Sigma-Aldrich) and ethylene carbonate (99% anhydrous) (Sigma-Aldrich). 1 M lithium bis(trifluoromethanesulfonyl)imide (LiTFSI) (99.95% trace metal basis) (Sigma-Aldrich) is used as lithium salt. The SBE solution is cured with a thermal initiator of 1 wt% 2,2'-azobis(2-methylpropionitrile) (AIBN) to the monomer weight (Sigma-Aldrich). The solution was stirred until a homogeneous mixture was obtained.

Table 1 Shortest distances and geodesic tortuosity of the SBE in dense graphs and sparse graphs, respectively.

	Dense graph study			Sparse graph study		
	Euclidean distance	Mean shortest distance	Geodesic tortuosity	Euclidean distance	Mean shortest distance	Geodesic tortuosity
x-direction	5.36	9.61	1.79	5.36	7.59	1.84
y-direction	6.32	11.28	1.81	6.32	8.67	1.81
z-direction	1.10	1.90	1.72	1.13	1.52	1.75

The geodesic tortuosity from the sparse graph considers segment tortuosity.

Table 2 The elastic modulus and lithium-ion conductivity of the bulk polymer, the liquid electrolyte, and the SBE.

	Experimental results			Simulation results
	Bulk polymer	Liquid electrolyte	SBE	SBE
Elastic modulus [MPa]	2167	-	611	738
Ionic conductivity [mS/cm]	-	4.35	0.134	0.633

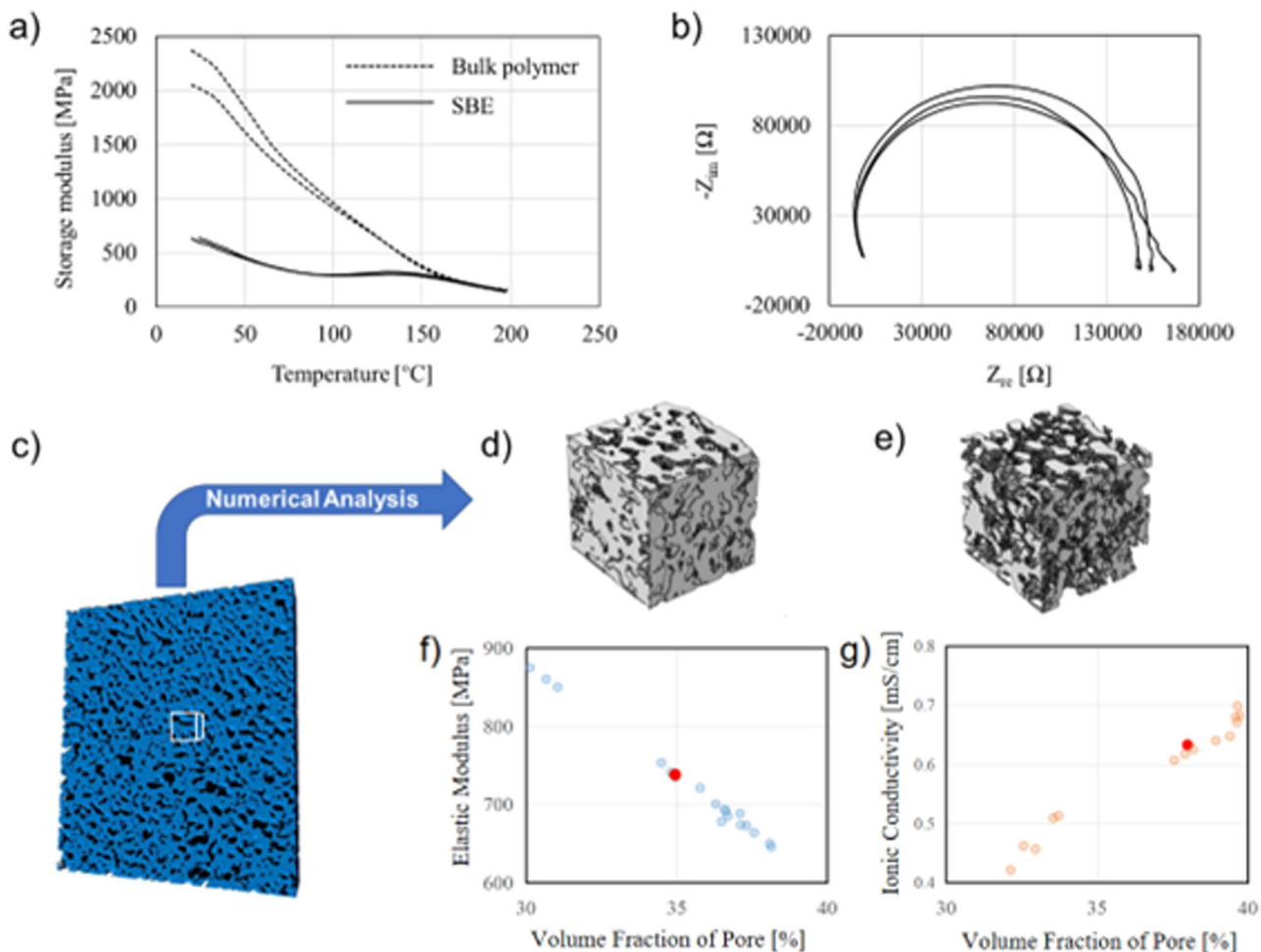


Fig. 5 Multifunctional performance of the SBE. Storage modulus and ionic conductivity of SBE. **a** Storage modulus measured by DMA for the bulk polymer and SBE. **b** Nyquist plot of EIS data for the SBE. **c** 20 SVEs were extracted from the 3D reconstructed model. Two SVEs of **d** the polymer and **e** the liquid electrolyte domains, respectively. The geometries are slightly defeatured for FEM simulation. The geometric dimensions of the SVEs are $1.18 \times 1.22 \times 1.18 \mu\text{m}^3$. FEM simulation results from all SVEs for **f** elastic modulus and **g** ionic conductivity. Each data point corresponds to one SVE simulation; the red dot represents the final average result.

The SBE resin was then poured into an aluminum mold ($30 \times 6 \times 0.5 \text{ mm}^3$) and covered with a glass slab. The specimens were subsequently clamped on both edges and vacuum-sealed into a pouch bag inside the glovebox. Finally, the samples were transferred outside the glovebox and directly thermally cured at 90°C for 45 min in a preheated oven. For the bulk polymer sample, the monomer was mixed with the AIBN only. The AIBN content was again 1 wt% of the monomer weight. The molds and the curing conditions were exactly the same as for the SBE films.

FIB-SEM. The samples were immersed in deionized water for 24 h and put on a shaking table to extract the liquid electrolyte (EC, PC, and LiTFSI) contained within the percolating polymer network. After that, the samples were dried in a vacuum oven for 48 h at 60°C . All samples were weighed before immersion in deionized water and after drying to determine the mass loss. The average mass loss corresponds to 42.34 wt %. An average of 5.9 wt% of liquid electrolyte was left. A $\sim 2 \text{ mm}^3$ SBE sample was glued on an aluminum stub with conductive silver paint. A 20 nm gold layer was then coated on the surface to increase the electric conductivity. FIB-SEM milling and imaging was performed in a Tescan GAIA3 (Tescan, Brno, Czech Republic). 30 keV Ga^+ ion beam was used in this study. Only the beam current varies at different steps. The specimen was first tilted 55° to the electron beam. About $2 \mu\text{m}$ thick platinum layer was deposited on an area of $10 \times 20 \mu\text{m}^2$ using 500 pA ion beam current. A T-shape section was then fabricated using 1 nA beam current as shown in Fig. 1b. A reference pattern was milled on the T-shape and used to compensate the sample drifts for FIB milling and SEM imaging. Milling was performed using a low ion beam current of 269 pA every 20 nm. High-resolution images were taken under electron immersion mode with a pixel size of $10 \times 10 \text{ nm}^2$. The electron beam spot size was set as 4 nm. The electron immersion mode introduces an electromagnetic field to cage all electrons. Therefore, a stronger electron accumulation effect causes sample drifting, which strongly limits the available image number. Here, 80 images are obtained before the reference pattern drifts out of the reference window. Sixty images are used for 3D reconstruction. The SEM images are taken using the Mid-angle backscattered electron detector to reduce the charging effect. The electron beam voltage is set as 2 keV.

Image processing. Once the SEM images were obtained, different image processing methods were used including filtering, registration, and segmentation. All these operations were performed using the Dragonfly 2020.2 software (Object Research Systems (ORS) Inc., Montreal, Canada, 2020). To reduce the artifacts in the original SEM images, filtering was used. The vertical stripes caused by a curtaining effect are reduced by destriping filtering. Since the curtaining artifact is similar to the stripe noise in remote sensing, different destriping methods developed over the years can be used, such as moment matching based method³³, histogram-based method³⁴, Fourier-based filtering methods^{35,36}, wavelet analysis methods^{37,38} and compression sensing method³⁹. Here a wavelet analysis method is chosen, where *Daubechies 5* wavelet (db5) was selected at level 5. The foreground pixel size is chosen as 128 and the background pixel size is chosen as 256. Furthermore, a Gaussian smoothing filter was then applied in 3D space with a sigma value of 3 to remove the noise pixels. Registration was then performed to realign images using the simple sum of squared differences (SSD) method according to Eq. 1.

$$\text{SSD} = \sum_{\text{pixel}} (\text{image1} - \text{image2})^2 \quad (1)$$

The method minimizes the SSD by realigning the images. This operation is repeated six times in a selected box region. Threshold segmentation was then performed to identify polymer and pore phases. The threshold value is gradually increased until the porosity of the 3D model is equal to the theoretical porosity calculated from the liquid phase in the SBE mixture. All polymer pixels are labeled 1 and pore pixels are labeled 0. Since most polymer and pore phases are connected, watershed segmentation was used to separate individual polymers and pores before the statistical analysis. The watershed algorithm treats a grayscale image as a topographic map where a brighter pixel represents a higher position, as illustrated in Fig. 3f⁴⁰. The ridges represent the boundaries of each catchment basin. The watershed segmentation was implemented using the OpenPNM plugin. OpenPNM is a free Python package that is built-in in the Dragonfly software and designed for pore network modeling (PNM). Here, OpenPNM is only used to generate the multi-ROI. For this purpose, OpenPNM uses a marked-based watershed algorithm to define individual elements⁴¹. Marked-based watershed finds the seeds of individual pore centers using a distance map (Fig. 3c), where the pixel grayscale value represents the minimum Euclidean distance from the pixel to the polymer. A pixel with a local maximum grayscale value is marked as a pore center. The local area is defined by a maximum spherical radius R_{max} . In this work, the R_{max} is set to 6 pixels.

Dynamic mechanical analysis. To evaluate the elastic modulus of the SBE, dynamic mechanical analysis (DMA) was performed. Here, DMA is used to measure the storage modulus of the SBE and bulk polymer. The instrument utilized was a TA Instruments DMA Q800 in tensile mode. In total, two samples for the SBE and two samples for the bulk polymer were tested. The samples were clamped into the DMA sample holder after having measured their width, thickness, and length between the clamps with a digital slide caliper. The specimen dimensions ranged between 4–5 mm in width, 0.4–0.55 mm in thickness, and 10–15 mm in length between the clamps. Specimen dimensions were inserted in the instrument program for analysis. The thermal cycle for the measurement consisted of a first

isothermal step where the initial temperature of 20°C was held for 10 min, needed for equilibration. The second step was a temperature ramp with a heating rate of 3°C min^{-1} up to a temperature of 200°C . An amplitude of 8–13 μm was applied ($<0.1\%$ of the sample length).

Electrochemical impedance spectroscopy. Electrochemical impedance spectroscopy (EIS) was executed for the evaluation of the ionic conductivity of the SBE at ambient temperature. The measurements were performed inside the glovebox immediately after the manufacture of the SBE films, avoiding liquid electrolyte evaporation from the samples. The analysis was conducted using a Gamry Series G 750 potentiostat/galvanostat/ZRA interface. The setup utilized consisted of a four-point electrode cell with gold wires as electrodes, two working electrodes (20 mm apart), and two reference electrodes (5 mm apart). In total, two samples were tested. The impedance was measured in the frequency range of 120 kHz to 1 Hz, with an amplitude of 10 mV. The bulk resistance (R_b) was obtained from the low-frequency intercept with the real axis in the resulting Nyquist plot. The ionic conductivity was calculated using Eq. 2:

$$\sigma = \frac{l}{R_b * A} \quad (2)$$

where σ is the ionic conductivity, l is the length between the reference electrodes (5 mm), R_b is the bulk resistance and A is the cross-sectional area of the sample. The cross-sectional area was calculated by measuring the thickness and width of each sample with a digital slide caliper.

Finite element method simulation. FEM simulation was implemented to perform virtual material testing via multi-scale computational homogenization using the model developed by ref. 32. Linear elasticity was used to compute the effective stiffness, while linear Fickian diffusion was assumed for the ionic conductivity. From the FIB-SEM data, a total of 20 unique statistical volume elements (SVEs) of each phase were generated. The SVE is a computational unit cell geometry that is supposed to represent the micro-heterogeneities of the SBE. The SVEs are voxel-based geometries that are generated by extruding either the white part or the black part of binarized 2D FIB-SEM images; this represents the liquid and the solid domain, respectively. The extrusion depth corresponds to the gap distance between each FIB-SEM image, i.e., 20 nm. The advantage of using a voxel-based geometry, in this case, is that a well-defined geometry, from experimental data, can easily be prepared for computer simulation. In fact, each voxel of the geometry is represented by a hexahedron element in the Finite Element simulations. The downside of voxel-based geometries is that they scale cubically in complexity with respect to the imaging resolution, resulting in computationally expensive FEM analyses. This issue can be circumvented by exploiting mesh reduction methods to reduce computational costs using a spatial voxel merging method⁴². However, spatial voxel merging is not pursued here as its interference with the porosity of the SBE is regarded as too defective. Instead, we accept the necessity of a fine mesh and resort to a high-performance computing cluster. The mesh generation was carried out in a small Python script. It should be noted that the SVE geometries are not periodic, therefore, periodic boundary conditions are not suitable here. Instead, Dirichlet boundary conditions were enforced on the fluctuation fields.

Data availability

The FIB-SEM image dataset used in this study can be found at <https://doi.org/10.5281/zenodo.8027406>. Any other information can be obtained from the corresponding author upon reasonable request.

Received: 24 March 2023; Accepted: 19 June 2023;

Published online: 29 June 2023

References

- Kim, T., Song, S., Son, D., Ono, L. & Qi, Y. Lithium-ion batteries: outlook on present, future, and hybridized technologies. *J. Mater. Chem. A* **7**, 2942 (2019).
- Asp, L. E., Johansson, M., Lindbergh, G., Xu, J. & Zenkert, D. Structural battery composites: a review. *Funct. Compos. Struct.* **1**, 0420001 (2019).
- Hegde, S., Shenoy, B. S. & Chethan, K. N. Review on carbon fiber reinforced polymer (CFRP) and their mechanical performance. *Mater. Today: Proc.* **19**, 658 (2019).
- Asp, L. E. et al. A structural battery and its multifunctional performance. *Adv. Energy Sustain. Res.* **2**, 2000093 (2021).
- Xu, J. et al. A multicell structural battery composite laminate. *EcoMat.* **4**, e12180 (2022).
- Johannisson, W. et al. Multifunctional performance of a carbon fiber UD lamina electrode for structural batteries. *Compos. Sci. Technol.* **168**, 81 (2018).
- Carlstedt, D. & Asp, L. E. Performance analysis framework for structural battery composites in electric vehicles. *Compos. B. Eng.* **186**, 107822 (2020).

8. Jin, T., Singer, G., Liang, K. & Yang, Y. Structural batteries: advances, challenges and perspectives. *Mater. Today* **62**, 151–167 (2023).
9. Carlstedt, D. et al. Experimental and computational characterization of carbon fibre based structural battery electrode laminae. *Compos. Sci. Technol.* **220**, 109283 (2022).
10. Hagberg, J. et al. Lithium iron phosphate coated carbon fibre electrodes for structural lithium ion batteries. *Compos. Sci. Technol.* **162**, 235–243 (2018).
11. Sanchez, J. S. et al. Electrophoretic coating of LiFePO₄/graphene oxide on carbon fibers as cathode electrodes for structural lithium ion batteries. *Compos. Sci. Technol.* **208**, 108768 (2021).
12. Zhao, Q., Sanjuna, S., Zhao, C. & Archer, L. A. Designing solid-state electrolytes for safe, energy-dense batteries. *Nat. Rev. Mater.* **5**, 229 (2020).
13. Snyder, J. F., Carter, R. H. & Wetzel, E. D. Electrochemical and mechanical behavior in mechanically robust solid polymer electrolytes for use in multifunctional structural batteries. *Chem. Mater.* **19**, 3793 (2007).
14. Schneider, L. M., Ihner, N., Zenkert, D. & Johansson, M. Bicontinuous electrolytes via thermally initiated polymerization for structural lithium ion batteries. *ACS Appl. Energy Mater.* **2**, 4362 (2019).
15. Le Houx, J. et al. Effect of tomography resolution on calculation of microstructural properties for lithium ion porous electrodes. *ECS Trans.* **97**, 255 (2020).
16. Joos, J., Carraro, T., Weber, A. & Tiffée, E. Reconstruction of porous electrodes by FIB/SEM for detailed microstructure modelling. *J. Power Sources* **196**, 7302 (2011).
17. Holzer, L., Indutnyi, F., Gasser, P. H., Münch, B. & Wegmann, M. Three-dimensional analysis of porous BaTiO₃ ceramics using FIB nanotomography. *J. Microsc.* **216**, 84 (2004).
18. Bassim, N., Scott, K. & Giannuzzi, L. A. Recent advances in focused ion beam technology and applications. *MRS Bull.* **39**, 317 (2014).
19. Fager, C. et al. 3D high spatial resolution visualisation and quantification of interconnectivity in polymer films. *Int. J. Pharm.* **587**, 119622 (2020).
20. Fager, C. et al. Optimization of FIB-SEM tomography and reconstruction for soft, porous, and poorly conducting materials. *Microsc. Microanal.* **26**, 837 (2020).
21. Deng, B. et al. FIB/SEM tomography of wound biofilm. *Microsc. Microanal.* **21**, 205 (2015).
22. Wolff, A. et al. FIB/SEM processing of biological samples. *Microsc. Microanal.* **24**, 822 (2018).
23. Neusser, G. et al. FIB and MIP: understanding nanoscale porosity in molecularly imprinted polymers via 3D FIB/SEM tomography. *Nanoscale* **9**, 14327–14334 (2017).
24. Giannuzzi, L. A. & Stevie, F. A. *Introduction to Focused Ion Beams* (Springer, 2005).
25. Giannuzzi, L. A. & Stevie, F. A. A review of focused ion beam milling techniques for TEM sample preparation. *Microsc. Microanal.* **30**, 197 (1999).
26. Lemmens, H. J., Butcher, A. R. & Botha, P. W. S. K. FIB/SEM and SEM/EDX: a new dawn for the SEM in the core lab? *Petrophysics* **52**, 452 (2011).
27. Liu, S., Sun, L., Gao, J. & Li, K. A fast curtain-removal method for 3D FIB-SEM images of heterogeneous minerals. *J. Microsc.* **272**, 3 (2018).
28. Ambroz, F., Macdonald, T. J., Martis, V. & Parkin, I. P. Evaluation of the BET theory for the characterization of meso and microporous MOFs. *Small Methods* **2**, 1800173 (2018).
29. Thommes, M. et al. Physisorption of gases, with special reference to the evaluation of surface area and pore size distribution (IUPAC Technical Report). *Pure Appl. Chem.* **87**, 1051–1069 (2015).
30. Cattaruzza, M. et al. Hybrid polymer–liquid lithium ion electrolytes: effect of porosity on the ionic and molecular mobility. *J. Mater. Chem. A* **11**, 7006–7015 (2023).
31. Gostick, J. et al. OpenPNM: a pore network modeling package. *Comput. Sci. Eng.* **18**, 60 (2016).
32. Tu, V. et al. Performance of bicontinuous structural electrolytes. *Multifunct. Mater.* **3**, 025001 (2020).
33. Gadallah, F. L., Csillag, F. & Smith, E. J. M. Destriping multisensor imagery with moment matching. *Int. J. Remote Sens.* **21**, 2505 (2000).
34. Rakwatin, P., Takeuchi, W. & Yasuoka, Y. Stripe noise reduction in MODIS data by combining histogram matching with facet filter. *IEEE Trans. Geosci. Remote Sens.* **45**, 1844 (2007).
35. Chen, S.-W. & Pellequer, J.-L. DeStripe: frequency-based algorithm for removing stripe noises from AFM images. *BMC Struct. Biol.* **11**, 1 (2011).
36. Chen, J., Shao, Y., Guo, H., Wang, W. & Zhu, B. Destriping CMODIS data by power filtering. *IEEE Trans. Geosci. Remote Sens.* **41**, 2119 (2003).
37. Torres, J. & Infante, S. O. Wavelet analysis for the elimination of striping noise in satellite images. *Opt. Eng.* **40**, 1309 (2001).
38. Münch, B., Trtik, P., Marone, F. & Stampanoni, M. Stripe and ring artifact removal with combined wavelet—Fourier filtering. *Opt. Express* **17**, 8567 (2009).
39. Schwartz, J. et al. Removing stripes, scratches, and curtaining with non-recoverable compressed sensing. *Microsc. Microanal.* **25**, 174 (2019).
40. Beucher, S. & Meyer, F. *Mathematical Morphology in Image Processing* (Marcel Dekker Inc., 1993).
41. Gostick, J. T. Versatile and efficient pore network extraction method using marker-based watershed segmentation. *Phys. Rev. E* **96**, 023307 (2017).
42. Auenhammer, R. M. et al. Robust numerical analysis of fibrous composites from X-ray computed tomography image data enabling low resolutions. *Compos. Sci. Technol.* **224**, 109458 (2022).

Acknowledgements

The project is funded by the USAF via the EOARD Award No. FA8655-21-1-7038, ONR, USA, Award No. N62909-22-1-2037, the Swedish National Space Agency, project no. 2020-00256, and the Swedish Energy Agency, grant #48488-1.

Author contributions

S.D. performed the FIB/SEM experiment, 3D reconstruction, and topological analysis, M.C. proposed the FIB/SEM, synthesis of the SBE and performed the DMA and EIS experiments, R.M.A. transferred the voxel model to FE mesh and V.T. conducted the FE simulations. L.E.A., F.L., M.K.G.J., and R.J. take part in the results discussion and interpretation. S.D. and L.E.A. wrote the original manuscript. All authors contributed to the results interpolation and writing the manuscript.

Funding

Open access funding provided by Chalmers University of Technology.

Competing interests

The authors declare no competing interests.

Additional information

Supplementary information The online version contains supplementary material available at <https://doi.org/10.1038/s43246-023-00377-0>.

Correspondence and requests for materials should be addressed to Leif E. Asp.

Peer review information *Communications Materials* thanks the anonymous reviewers for their contribution to the peer review of this work. Primary Handling Editor: Jet-Sing Lee. A peer review file is available.

Reprints and permission information is available at <http://www.nature.com/reprints>

Publisher's note Springer Nature remains neutral with regard to jurisdictional claims in published maps and institutional affiliations.



Open Access This article is licensed under a Creative Commons Attribution 4.0 International License, which permits use, sharing, adaptation, distribution and reproduction in any medium or format, as long as you give appropriate credit to the original author(s) and the source, provide a link to the Creative Commons license, and indicate if changes were made. The images or other third party material in this article are included in the article's Creative Commons license, unless indicated otherwise in a credit line to the material. If material is not included in the article's Creative Commons license and your intended use is not permitted by statutory regulation or exceeds the permitted use, you will need to obtain permission directly from the copyright holder. To view a copy of this license, visit <http://creativecommons.org/licenses/by/4.0/>.

© The Author(s) 2023